

Numerical simulations of global approach for photon scanning tunneling microscopy: coupling of finite-element and boundary integral methods

Peijun Li

*Department of Mathematics, University of Michigan, Ann Arbor, Michigan 48109, USA
(lpeijun@umich.edu)*

Received March 20, 2008; revised May 28, 2008; accepted June 8, 2008;
posted June 10, 2008 (Doc. ID 94072); published July 8, 2008

An accurate global model is proposed for a two-dimensional probe-sample system of photon scanning tunneling microscopy in near-field optics. A coupling of a finite-element method in the inhomogeneous sample and a boundary integral method on the artificial boundary of the truncated domain is developed. Numerical experiments are included to demonstrate the effectiveness of the proposed method and to show the features of wave propagation in photon scanning tunneling microscopy. © 2008 Optical Society of America

OCIS codes: 000.4430, 180.4243, 180.5810, 290.2558.

1. INTRODUCTION

Scattering problems are basic in many scientific areas such as radar and sonar, geophysical exploration, and medical imaging [1]. However, there is a resolution limit to the sharpness of details that can be observed by conventional far-field optical microscopy, one half the wavelength, referred to as the diffraction limit [2,3]. Near-field optics provides an effective approach to breaking the diffraction limit and obtaining images with subwavelength resolution, which has been experimentally observed [4,5]. Because of this fascinating feature, it has developed dramatically in recent years and been applied in diverse aspects, including near-field optical microscopy, nondestructive imaging of small-scale biological samples, and nanotechnology [6].

In order to theoretically understand the physical mechanism of this capability, it is desirable to accurately solve the underlying scattering problem for near-field optics. The objective of this paper is to investigate the mathematical modeling of the scattering problem for one of the important experimental modes in near-field optics, photon scanning tunneling microscopy (PSTM) [7–9]. In this mode, as seen in Fig. 1, a sample is illuminated by an evanescent wave generated at the face of a prism from the total internal reflection [10], and the wave field above the prism is scanned by passing a tapered fiber probe over the sample in the near-field zone with a constant height configuration. To resolve the small-scale features present in near-field optics applications, precise modeling and an accurate solution for the electromagnetic fields are required.

A number of models based on global [11–15] and local [16–18] approaches have been developed in order to describe the probe-sample system for the PSTM configuration. Regarding local approaches, the wave field above a

prism can be modeled without taking into account the probe. Such approaches are valid only if the probe influence can be considered as a small perturbation to the wave field excited by sample. The global approaches, including both probe and sample, are necessary when the probe-sample interaction is strong. There have been many numerical methods based on global approaches, such as the Green's functions method [19,20], the multiple multipole method [21], the finite-element or finite-difference method [22], and the boundary integral method [23]. These models reflect the nature of the electromagnetic confinement around the tip probe, and associated numerical methods can thus efficiently treat the electromagnetic field scattering at the probe apex. However, they are difficult to use to compute all the fields coupled to the propagating mode in the fiber probe. Recently, a global model with an R -matrix algorithm incorporated into the Fourier modal method has been developed [24,25], where a periodic structure of the probe-sample system is assumed.

In this paper, we propose an accurate global model and develop a coupling of the finite-element and boundary integral methods for numerical simulations of the interaction between subwavelength sample and probe. We make no assumptions about the physical system and consider extremely general material properties for the sample and probe, whose refractive indices need only to be bounded functions. Variational formulations for coupling a finite-element method in the inhomogeneous sample with a boundary integral method on the artificial boundary of the truncated domain are studied. Numerical experiments are included to demonstrate the effectiveness of the proposed method and to show the features of wave propagation in PSTM. Since the proposed model and method have no limitations on the optical or geometrical

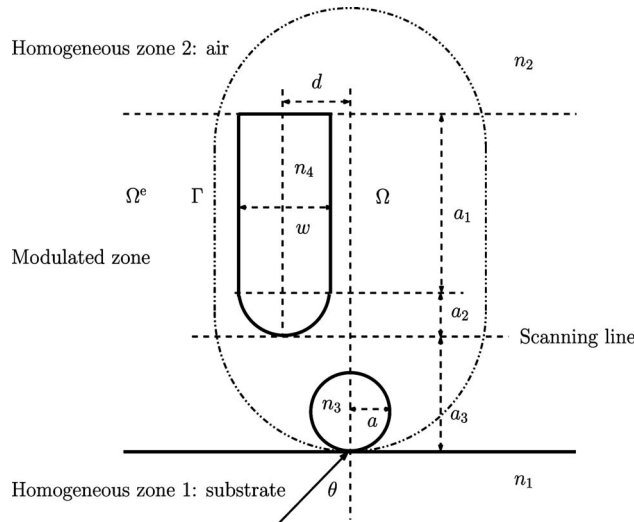


Fig. 1. Geometry of the model: Photon scanning tunneling microscopy. The probe length is a_1+a_2 , where a_1 is the length of a rectangular part, a_2 is the radius of a semi-disc-shaped taper, and w is the probe width. The probe-substrate distance is a_3 ; n_1, n_2, n_3 , and n_4 are the refractive indices of the respective media.

parameters of the probe and sample, it can be used for realistic simulations of various near-field microscope configurations.

2. MODEL PROBLEM

Consider an inhomogeneous sample deposited on a homogeneous substrate. The sample is illuminated from below (transmission geometry) by a time-harmonic plane wave, as shown in Fig. 1. Throughout, by assuming nonmagnetic materials and transverse electric polarization, we study a two-dimensional system with three different zones. The first zone corresponds to the substrate and is assumed to be semi-infinite and homogenous with a constant refractive index n_1 . The second zone is the modulated zone, which includes the sample and the probe with refractive indices n_3 and n_4 , respectively. The third one is a homogenous air zone with a constant refractive index n_2 . The model probe consists of a rectangular part with length a_1 and width w , followed by a semi-disc-shaped taper with radius $a_2=w/2$. The displacement distance d is the x_1 direction distance between the center axis of the probe and the center axis of the sample. The sign d is positive when the probe is on the right-hand side of the sample and negative otherwise.

Specifically, let an incoming plane wave $u^i = \exp(i\alpha x_1 + i\beta x_2)$ be incident on the straight line $\{x_2=0\}$ from $\mathbb{R}_-^2 = \{\mathbf{x}: x_2 < 0\}$, where $\alpha = n_1 \kappa_0 \sin \theta$, $\beta = n_1 \kappa_0 \cos \theta$, $\theta \in (-\pi/2, \pi/2)$ is the angle of incidence, and κ_0 is the free-space wavenumber. The total field u satisfies the Helmholtz equation

$$\Delta u + \kappa^2 n^2 u = 0 \quad \text{in } \mathbb{R}^2, \tag{1}$$

where $n(\mathbf{x})$ is the index of refraction, which varies within the domain of the sample and the probe but otherwise has a value of unity, and the wavenumber is

$$\kappa(\mathbf{x}) = \begin{cases} \kappa_0 & \text{for } x_2 > 0 \\ n_1 \kappa_0 & \text{for } x_2 < 0 \end{cases}.$$

Denote the reference field u^{ref} as the solution of the homogeneous equation

$$\Delta u^{\text{ref}} + \kappa^2 u^{\text{ref}} = 0 \quad \text{in } \mathbb{R}^2. \tag{2}$$

It can be shown from Eq. (2) together with continuity conditions that

$$u^{\text{ref}} = \begin{cases} u^t & \text{for } x_2 > 0 \\ u^i + u^r & \text{for } x_2 < 0 \end{cases},$$

where u^t and u^r are the transmitted and reflected waves, respectively. More precisely, we have

$$u^t = t \exp(i\alpha x_1 + i\gamma x_2), \quad u^r = r \exp(i\alpha x_1 - i\beta x_2), \tag{3}$$

where $t = 2\beta/(\beta + \gamma)$, $r = (\beta - \gamma)/(\beta + \gamma)$, and

$$\gamma(\alpha) = \begin{cases} \sqrt{\kappa_0^2 - \alpha^2} & \text{for } \kappa_0 > |\alpha| \\ i\sqrt{\alpha^2 - \kappa_0^2} & \text{for } \kappa_0 < |\alpha| \end{cases}. \tag{4}$$

It is easily seen from Eqs. (3) and (4) that when the incident angle is greater than the critical angle, i.e., when $\kappa_0 < |\alpha|$, the function $\gamma(\alpha)$ is purely imaginary. The transmitted wave becomes an evanescent wave, which propagates on the substrate surface in the x_1 direction but exponentially decays in the x_2 direction.

The total field consists of the reference field u^{ref} and the scattered field u^s :

$$u = u^{\text{ref}} + u^s. \tag{5}$$

In addition, the scattered field is required to satisfy the following radiation condition:

$$\lim_{\rho \rightarrow \infty} \int_{\Sigma_\rho} \left| \frac{\partial u^s}{\partial \nu} - i\kappa u^s \right|^2 ds = 0, \tag{6}$$

where Σ_ρ is the circle of radius ρ and ν is the unit outward normal to Σ_ρ .

We shall use the following notations: For a bounded region Ω in \mathbb{R}^2 with boundary Γ , $H^s(\Omega)$ and $H^s(\Gamma)$ will denote the usual Sobolev spaces with norm $\|\cdot\|_s$ and $|\cdot|_s$, respectively.

3. COUPLING OF FINITE-ELEMENT AND BOUNDARY INTEGRAL METHODS

To apply a numerical method, the open physical domain needs to be truncated into a bounded computational domain. Therefore, a suitable boundary condition has to be imposed on the boundary of the bounded domain so that no artificial wave reflection occurs. Here we present a boundary integral method for the truncated domain combined with a finite-element method in the inhomogeneous sample. The coupling of finite-element and boundary integral methods has proved to be one of the most popular and efficient methods for problems posed on an unbounded domain [26–29]. Since we are concerned mainly with the wave field above the substrate, we may let $\Omega \subseteq \mathbb{R}_+^2$, containing the sample, be a Lipschitz continuous bounded domain with boundary Γ , and let $\Omega^e = \mathbb{R}^2 \setminus \bar{\Omega}$ be

the exterior of Ω , as seen in Fig. 1. In the following, we derive variational formulations for the coupling procedure.

Let λ be the normal derivative of the total field on the boundary Γ . The model problem formulated in the open domain in Section 2 can be reduced to one in a bounded domain:

$$\Delta u + \kappa^2 n^2 u = 0 \quad \text{in } \Omega, \quad (7)$$

$$\frac{\partial u}{\partial \nu} = \lambda \quad \text{on } \Gamma. \quad (8)$$

We shall first give a variational formulation of Eqs. (7) and (8).

Let $\langle \cdot, \cdot \rangle$ denote the duality between $H^1(\Omega)$ and $H^{-1}(\Omega)$, the dual space of $H^1(\Omega)$, with

$$\langle \varphi, \psi \rangle = \int_{\Omega} \varphi \bar{\psi} d\mathbf{x},$$

and $\langle \cdot, \cdot \rangle$ denote the duality between $H^{1/2}(\Gamma)$ and $H^{-1/2}(\Gamma)$, the dual space of $H^{1/2}(\Gamma)$, with

$$\langle \varphi, \psi \rangle = \int_{\Gamma} \varphi \bar{\psi} ds,$$

where the overbar is the complex conjugate. The problem of Eqs. (7) and (8) has an equivalent variational form: Find $u \in H^1(\Omega)$ such that

$$a(u, v) - \langle \lambda, v \rangle = 0 \quad \text{for all } v \in H^1(\Omega), \quad (9)$$

where the bilinear form is defined by

$$a(u, v) = (\nabla u, \nabla v) - (\kappa^2 n^2 u, v).$$

Equation (9) is underdetermined since both u and λ are unknowns. We next present a boundary integral equation and its variational formulation, which provides a relation between the field u and its normal derivative λ .

Consider the scattered field in the exterior domain Ω^e ,

$$\Delta u^s + \kappa^2 u^s = 0 \quad \text{in } \Omega^e. \quad (10)$$

Based on Eq. (10) and the radiation condition (6), it follows from Green's theorem and jump relations for surface potentials that the scattered field satisfies the integral equation

$$\begin{aligned} \frac{1}{2} u^s(\mathbf{x}) &= \int_{\Gamma} \frac{\partial G(\mathbf{x}, \mathbf{y})}{\partial \nu(\mathbf{y})} u^s(\mathbf{y}) ds(\mathbf{y}) \\ &- \int_{\Gamma} G(\mathbf{x}, \mathbf{y}) \frac{\partial u^s(\mathbf{y})}{\partial \nu(\mathbf{y})} ds(\mathbf{y}) \quad \mathbf{x} \in \Gamma, \end{aligned} \quad (11)$$

where $G(\mathbf{x}, \mathbf{y}) = \Phi_1(\mathbf{x}, \mathbf{y}) + \Psi_1(\mathbf{x}, \mathbf{y})$ is the fundamental solution for the Helmholtz equation in a two-layered background medium, given in Appendix A. The function Φ_1 is the fundamental solution of the Helmholtz equation in a homogeneous background with wavenumber κ_0 , and Ψ_1 is a smooth function accounting for reflection due to the layered background.

Regarding the reference field in Ω , we have again from Green's theorem and jump relations that

$$\begin{aligned} \frac{1}{2} u^{\text{ref}}(\mathbf{x}) &= - \int_{\Gamma} \frac{\partial G(\mathbf{x}, \mathbf{y})}{\partial \nu(\mathbf{y})} u^{\text{ref}}(\mathbf{y}) ds(\mathbf{y}) \\ &+ \int_{\Gamma} G(\mathbf{x}, \mathbf{y}) \frac{\partial u^{\text{ref}}(\mathbf{y})}{\partial \nu(\mathbf{y})} ds(\mathbf{y}), \quad \mathbf{x} \in \Gamma. \end{aligned} \quad (12)$$

Combining Eqs. (11) and (12) leads to an integral equation for the total field

$$\begin{aligned} u(\mathbf{x}) &= 2 \int_{\Gamma} \frac{\partial G(\mathbf{x}, \mathbf{y})}{\partial \nu(\mathbf{y})} u(\mathbf{y}) ds(\mathbf{y}) - 2 \int_{\Gamma} G(\mathbf{x}, \mathbf{y}) \frac{\partial u(\mathbf{y})}{\partial \nu(\mathbf{y})} ds(\mathbf{y}) \\ &+ 2u^{\text{ref}}(\mathbf{x}), \quad \mathbf{x} \in \Gamma. \end{aligned} \quad (13)$$

We introduce a single-layer potential operator

$$(S\varphi)(\mathbf{x}) := 2 \int_{\Gamma} G(\mathbf{x}, \mathbf{y}) \varphi(\mathbf{y}) ds(\mathbf{y}) \quad (14)$$

and a double-layer potential operator

$$(D\varphi)(\mathbf{x}) := 2 \int_{\Gamma} \frac{\partial G(\mathbf{x}, \mathbf{y})}{\partial \nu(\mathbf{y})} \varphi(\mathbf{y}) ds(\mathbf{y}). \quad (15)$$

Using these operators, Eq. (13) can be written as

$$u - Du + S\lambda = 2u^{\text{ref}} \quad \text{on } \Gamma. \quad (16)$$

Multiplying Eq. (16) by the complex conjugate of μ and integrating over Γ , it follows that

$$\langle u, \mu \rangle - \langle Du, \mu \rangle + \langle S\lambda, \mu \rangle = \langle 2u^{\text{ref}}, \mu \rangle, \quad \mu \in H^{-1/2}(\Gamma).$$

Hence if u is the solution of Eqs. (7) and (8), then the pair of functions $[u, \lambda]$ gives a solution of the variational problem: Find $[u, \lambda] \in H^1(\Omega) \times H^{-1/2}(\Gamma)$ such that

$$a(u, v) - \langle \lambda, v \rangle = 0 \quad \text{for all } v \in H^1(\Omega), \quad (17)$$

$$\langle u, \mu \rangle - \langle Du, \mu \rangle + \langle S\lambda, \mu \rangle = \langle 2u^{\text{ref}}, \mu \rangle \quad \text{for all } \mu \in H^{-1/2}(\Gamma). \quad (18)$$

Next we present the discrete problem for the coupled variational approximation, on which the numerical method is based.

Let $\mathbf{x}(t)$ be a parametrization of the boundary Γ , where $0 \leq t \leq 1$. Given any parameter $h \in (0, 1]$, let $0 = t_0 \leq t_1 \leq \dots \leq t_N = 1$ be a partition of $[0, 1]$ with $t_{i+1} - t_i = h_i < h$ for $i = 0, \dots, N-1$. We denote by Ω_h the polygonal domain that approximates Ω with vertices $\{\mathbf{x}(t_i), i = 1, \dots, N\}$ on the boundary Γ . Let $\tilde{\mathcal{T}}_h$ be a regular triangulation of $\bar{\Omega}_h$ by triangles \tilde{T} with diameter $h_{\tilde{T}}$ no greater than h . We thus obtain from $\tilde{\mathcal{T}}_h$ a triangulation \mathcal{T}_h of $\bar{\Omega}$, replacing each triangle $\tilde{T} \in \tilde{\mathcal{T}}_h$ with one side along a curved part of Γ with the corresponding curved triangle T , which leads to $\Omega = \cup_{T \in \mathcal{T}_h} T$.

Define a conforming finite-element subspace of $H^1(\Omega)$,

$$X_h = \{u \in H^1(\Omega) : u|_T \text{ is linear, } T \in \mathcal{T}_h\}.$$

Let Y_h be the space of 1-periodic piecewise constant functions on the partition: $0 = t_0 \leq t_1 \leq \dots \leq t_N = 1$. It is known that Y_h is a subspace of $H^{-1/2}(\Omega)$ [30]. We are now in a

position to write the discrete problem: Find $[u_h, \lambda_h] \in X_h \times Y_h$ such that

$$a(u_h, v) - \langle \lambda_h, v \rangle = 0 \quad \text{for all } v \in X_h, \quad (19)$$

$$\langle u_h, \mu \rangle - \langle Du_h, \mu \rangle + \langle S\lambda_h, \mu \rangle = \langle 2u^{\text{ref}}, \mu \rangle \quad \text{for all } \mu \in Y_h. \quad (20)$$

4. NUMERICAL EXPERIMENTS

We report several examples to demonstrate the effectiveness of the proposed method and to show the features of wave propagation in PSTM. In all of the experiments, we used a He–Ne laser of wavelength $\lambda=632.8$ nm as the source and chose an angle of incident $\theta=60^\circ$. Refractive indices are taken as $n_1=n_3=n_4=1.458$ and $n_2=1$. Figure 2 shows the geometry of the computational domain with width 0.8λ (506.2 nm) and length 2.4λ (1518.6 nm) and an example of the triangulation. Here we adopt a simple and effective mesh generator implemented in Matlab by Persson and Strang [31]. To approximate the integrals related to the potential operators S and D in Eq. (20), we use the Galerkin method based on a subtraction of the logarithmic singularity, an exact computation of the singular part, and a simple midpoint quadrature rule for the remaining terms. For the regular boundary integrals in Eqs. (19) and (20), we use the midpoint rule. The integrals over triangles of \mathcal{T}_h are approximated with standard quadrature rules. In order to compute the improper integral for the function Ψ_1 , we break it into two parts: One has a singular kernel integrated over a finite interval, and another has an infinite upper limit but with an exponentially decayed kernel. The Gauss–Chebyshev quadrature is used to deal with the first part, while the composite trapezoidal rule is employed to approximate the second part. We employ the commonly used outward-looking approach [32] for the linear system from the discretization of Eqs. (19) and (20).

A. Example 1: Two-Layered Background Medium without a Sample or a Probe

To test the accuracy and convergence of the proposed method, as a first step we calculate the intensity of the total field formed only by the two-layered background medium, whose exact solution is given in Eq. (3). Figure 3 plots a log–log scale of the $H^1(\Omega)$ error $\|u - u_h\|_1$ versus the number of nodes N , which shows that the associated error follows $\|u - u_h\|_1 = \mathcal{O}(N^{-1/2})$ or $\|u - u_h\|_1 = \mathcal{O}(h)$. The surface plot of the intensity for the total field and its image view are shown in Figs. 4(a) and 4(b), respectively. As we can see, the total field above the surface of the substrate is an evanescent wave, whose intensity exponentially decays as a function of depth in the x_2 direction.

B. Example 2: Subwavelength Sample without a Probe

To compare differences of the intensity distributions with or without a probe and thus to understand the influence of a probe, we calculate the near-field pattern formed by the presence of a disc-shaped dielectric sample with radius 100 nm deposited on an infinitely thick substrate without a probe. From the given refractive index of the

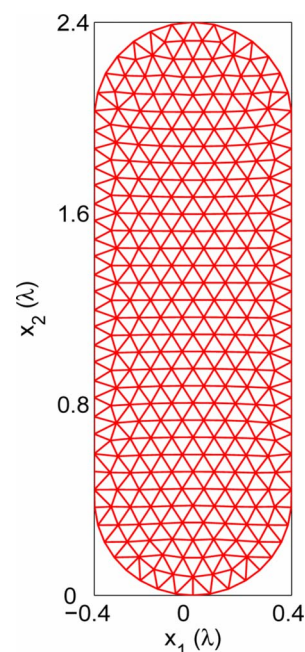


Fig. 2. (Color online) Geometry of the computational domain and a mesh.

substrate $n_1=1.458$ and incident angle $\theta=60^\circ$, it is obvious that the sample is illuminated in the total internal reflection configuration. Under the same configuration as Example 1, an evanescent wave is generated on the substrate surface. Due to the presence of a sample on the substrate surface, the interaction between the evanescent field and the sample produces a propagating wave, which is the photon tunneling effect. See Figs. 5(a) and 5(b) for the surface plot of the intensity for the total field and its image view, respectively.

C. Example 3: Subwavelength Sample with a Probe

Having analyzed the near-field pattern associated with the subwavelength sample on the substrate surface, we now consider the probe–sample system in order to analyze the influence of the probe on the intensity of the total field. The probe is positioned at a distance of $a_3=250$ nm from the substrate surface, which means that the probe–sample distance is 50 nm. The probe width is $w=200$ nm,

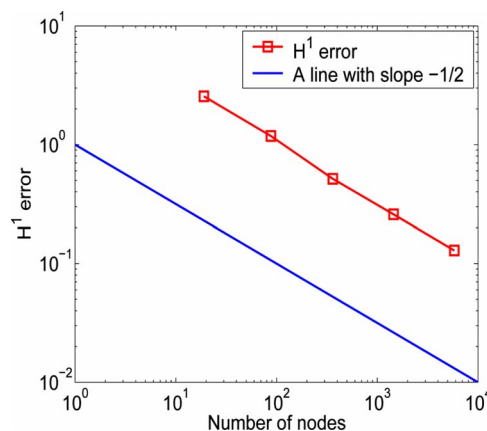


Fig. 3. (Color online) Example 1: The log–log scale of the error $\|u - u_h\|_1$ versus the number of nodes.

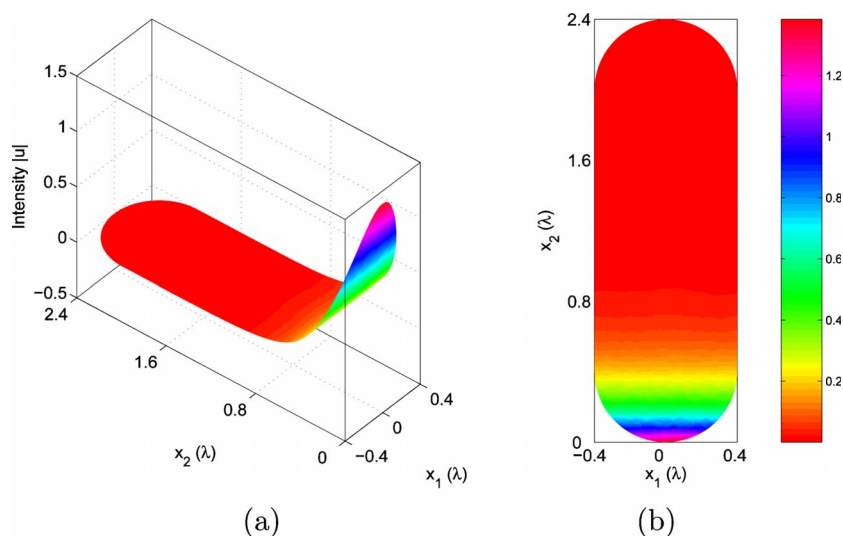


Fig. 4. (Color online) Intensity of the total field in Example 1: (a) The surface plot; (b) the image view.

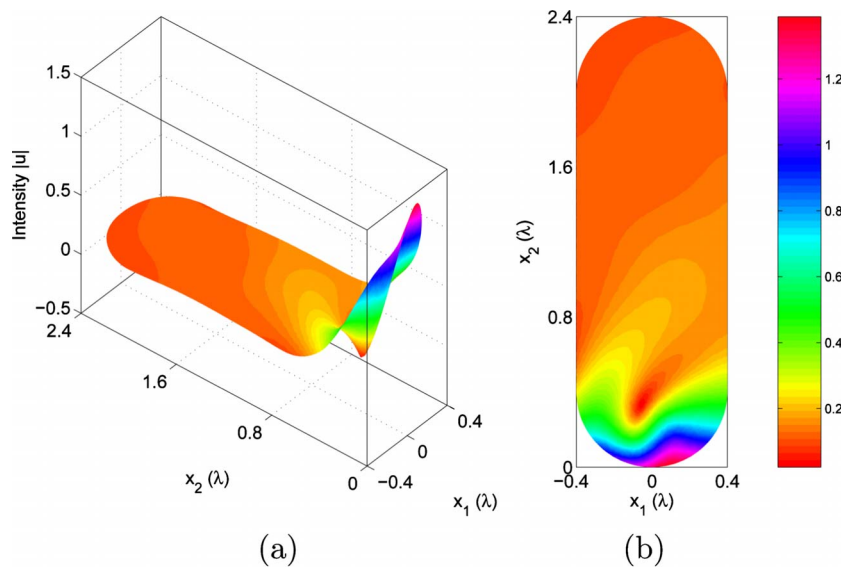


Fig. 5. (Color online) Intensity of the total field in Example 2: (a) The surface plot; (b) the image view.

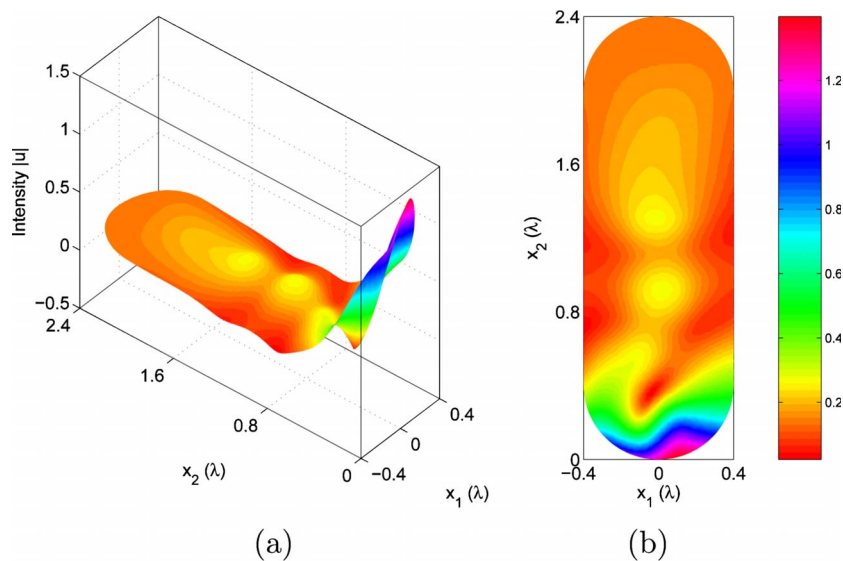


Fig. 6. (Color online) Intensity of the total field in Example 3: (a) The surface plot; (b) the image view.

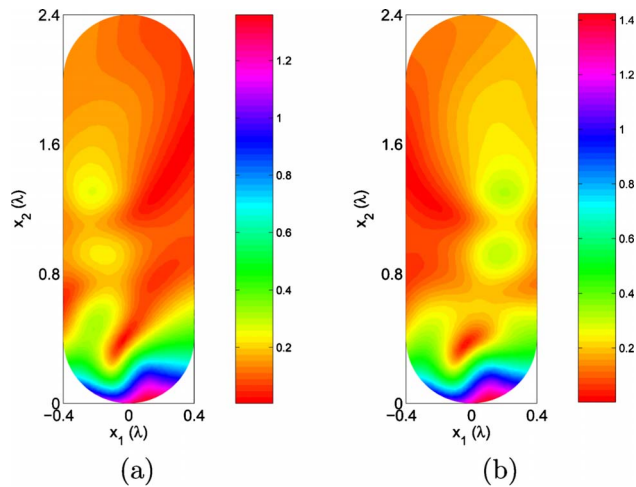


Fig. 7. (Color online) Intensity of the total field with displacement in Example 3: (a) $d = -100$ nm; (b) $d = 100$ nm.

and the length of the rectangular part is taken as $a_1 = 500$ nm. Thus the radius of the taper is $a_2 = 100$ nm, and the total length of the probe is $a_1 + a_2 = 600$ nm. The surface plot of the intensity for the total field and its image view are given in Figs. 6(a) and 6(b), respectively, when the probe is on top of the sample, i.e., the displacement distance $d = 0$. In contrast to the intensity distribution related to the sample in the absence of the probe, here a propagating wave is guided through the probe. To investigate the dependence of the intensity on the displacement distance, Figs. 7(a) and 7(b) plot the intensity for displacement distance $d = -100$ nm and $d = 100$ nm, respectively. It can be noticed that a propagating wave is detected and guided through the place where the probe is occupied.

D. Example 4: Subwavelength Sample with a Longer Probe

This example is to investigate the effect of the length of a probe on the intensity distribution. The probe width is maintained equal to $w = 200$ nm, and the sample radius is

kept to $a = 100$ nm as before. The probe–interface and the probe–sample distances are taken to $a_3 = 250$ nm and 50 nm, respectively. The rectangular part of the probe is $a_1 = 1000$ nm, and thus the total length of the probe is $a_1 + a_2 = 1100$ nm. The surface plot of the intensity for the total field and its image view are given in Figs. 8(a) and 8(b), respectively, when the probe is on top of the sample, i.e., the displacement distance $d = 0$. In contrast to the propagation wave through the probe with Example 3, here the detected propagation wave is guided through the whole probe with a larger length. The total field intensity dependence on the displacement distance is also shown in Figs. 9(a) and 9(b) for $d = -100$ nm and $d = 100$ nm, respectively. Once again, it can be noticed that a propagating wave is detected and guided through the place where the probe is occupied.

5. CONCLUSION

We have proposed an accurate global model of the probe–sample system for a PSTM configuration in near-field optics. Using the coupling of finite-element and boundary integral methods, we have presented the variational formulations of the underlying scattering problem for the two-dimensional Helmholtz equation with a two-layered background medium. Numerical experiments are included to demonstrate the effectiveness of the proposed method and to show the features of wave propagation in PSTM. The proposed model and method have no limitations on the physical system and can be used for realistic simulations of various near-field microscope configurations. It is currently being extended to study the influence of the taper shape, the presence of an apex with different sizes, and the metal-coated probe on the intensity distribution. To resolve these smaller-scale phenomena, a more sophisticated adaptive strategy needs to be employed for the method of coupling a finite element and a boundary integral.

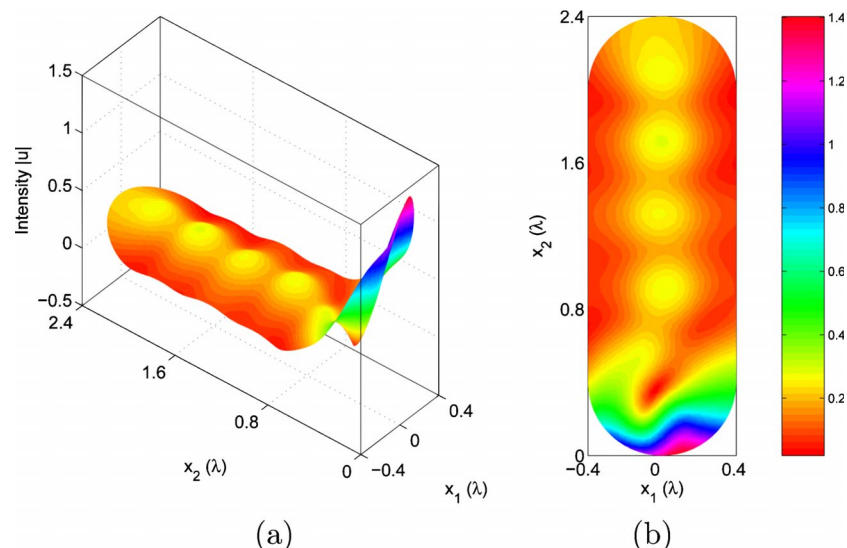


Fig. 8. (Color online) Intensity of the total field in Example 4: (a) The surface plot; (b) the image view.

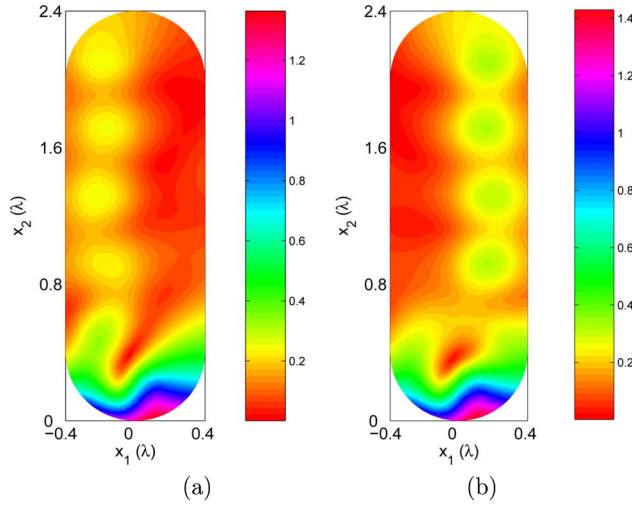


Fig. 9. (Color online) Intensity of the total field with displacement in Example 4: (a) $d = -100$ nm; (b) $d = 100$ nm.

APPENDIX A: TWO-LAYERED FUNDAMENTAL SOLUTION

For the observation point $\mathbf{x}=(x_1, x_2)$ and source point $\mathbf{y}=(y_1, y_2)$, the fundamental solution of the Helmholtz equation in a two-layered background medium in \mathbb{R}^2 satisfies

$$\Delta G(\mathbf{x}, \mathbf{y}) + \kappa^2(\mathbf{x})G(\mathbf{x}, \mathbf{y}) = -\delta(\mathbf{x} - \mathbf{y}), \quad (\text{A1})$$

with continuity conditions

$$G(\mathbf{x}, \mathbf{y})|_{x_2=0^+} = G(\mathbf{x}, \mathbf{y})|_{x_2=0^-}, \quad (\text{A2})$$

$$\left. \frac{\partial G(\mathbf{x}, \mathbf{y})}{\partial x_2} \right|_{x_2=0^+} = \left. \frac{\partial G(\mathbf{x}, \mathbf{y})}{\partial x_2} \right|_{x_2=0^-}, \quad (\text{A3})$$

where the wavenumber

$$\kappa(\mathbf{x}) = \begin{cases} \kappa_1 & \text{for } x_2 > 0 \\ \kappa_2 & \text{for } x_2 < 0 \end{cases}.$$

Define

$$\beta_i = \begin{cases} \sqrt{\kappa_i^2 - \xi^2} & \text{for } |\kappa_i| > |\xi| \\ i\sqrt{\xi^2 - \kappa_i^2} & \text{for } |\kappa_i| < |\xi| \end{cases}.$$

It follows from the Fourier transform that the fundamental solution is given by [33]

- $x_2 > 0, y_2 > 0$

$$G(\mathbf{x}, \mathbf{y}) = \Phi_1(\mathbf{x}, \mathbf{y}) + \Psi_1(\mathbf{x}, \mathbf{y}),$$

- $x_2 < 0, y_2 < 0$

$$G(\mathbf{x}, \mathbf{y}) = \Phi_2(\mathbf{x}, \mathbf{y}) + \Psi_2(\mathbf{x}, \mathbf{y}),$$

- $x_2 > 0, y_2 < 0$

$$G(\mathbf{x}, \mathbf{y}) = \Psi_3(\mathbf{x}, \mathbf{y}),$$

- $x_2 < 0, y_2 > 0$

$$G(\mathbf{x}, \mathbf{y}) = \Psi_4(\mathbf{x}, \mathbf{y}),$$

where

$$\Psi_1(\mathbf{x}, \mathbf{y}) = \frac{i}{4\pi} \int_{-\infty}^{\infty} \frac{1}{\beta_1} \frac{\beta_1 - \beta_2}{\beta_1 \beta_1 + \beta_2} e^{i\beta_1(x_2+y_2)} e^{i\xi(x_1-y_1)} d\xi, \quad (\text{A4})$$

$$\Psi_2(\mathbf{x}, \mathbf{y}) = \frac{i}{4\pi} \int_{-\infty}^{\infty} \frac{1}{\beta_2} \frac{\beta_2 - \beta_1}{\beta_2 \beta_1 + \beta_2} e^{-i\beta_2(x_2+y_2)} e^{i\xi(x_1-y_1)} d\xi, \quad (\text{A5})$$

$$\Psi_3(\mathbf{x}, \mathbf{y}) = \frac{i}{2\pi} \int_{-\infty}^{\infty} \frac{e^{i(\beta_1 x_2 - \beta_2 y_2)}}{\beta_1 + \beta_2} e^{i\xi(x_1-y_1)} d\xi, \quad (\text{A6})$$

$$\Psi_4(\mathbf{x}, \mathbf{y}) = \frac{i}{2\pi} \int_{-\infty}^{\infty} \frac{e^{i(\beta_1 y_2 - \beta_2 x_2)}}{\beta_1 + \beta_2} e^{i\xi(x_1-y_1)} d\xi, \quad (\text{A7})$$

and Φ_i is the fundamental solution of the Helmholtz equation in a homogeneous background medium in \mathbb{R}^2 with wavenumber κ_i , i.e.,

$$\Phi_i(\mathbf{x}, \mathbf{y}) = \frac{i}{4} H_0^{(1)}(\kappa_i |\mathbf{x} - \mathbf{y}|), \quad i = 1, 2.$$

Here $H_0^{(1)}$ is the Hankel function of the first kind with order zero.

ACKNOWLEDGMENTS

The author wishes to thank Gang Bao of Michigan State University and John Schotland of the University of Pennsylvania for valuable discussions, and Selim Esedoğlu of the University of Michigan for his support. The research was supported in part by a University of Michigan Research Fellowship and NSF EAR-0724656.

REFERENCES

1. D. Colton and R. Kress, *Inverse Acoustic and Electromagnetic Scattering Theory*, 2nd ed., Vol. 93 of the Applied Mathematical Sciences Series (Springer-Verlag, 1998).
2. D. Courjon, *Near-Field Microscopy and Near-Field Optics* (Imperial College Press, 2003).
3. C. Girard and A. Dereux, "Near-field optics theories," Rep. Prog. Phys. **59**, 657–699 (1996).
4. E. Betzig and J. K. Trautman, "Near-field optics: Microscopy, spectroscopy, and surface modification beyond the diffraction limit," Science **257**, 189–195 (1992).
5. D. Courjon and C. Bainier, "Near field microscopy and near field optics," Rep. Prog. Phys. **57**, 989–1028 (1994).
6. P. Carney and J. Schotland, "Near-field tomography," in *Inside Out: Inverse Problems and Applications*, G. Uhlmann, ed. (Cambridge U. Press, 2003), pp. 133–168.
7. G. Binnig and H. Rohrer, "Scanning tunneling microscopy," Helv. Phys. Acta **55**, 726–735 (1982).
8. D. Courjon, K. Sarayeddine, and M. Spajer, "Scanning tunneling optical microscopy," Opt. Commun. **71**, 23–28 (1989).
9. P. Carney and J. Schotland, "Determination of three-dimensional structure in photon scanning tunneling microscopy," J. Opt. A, Pure Appl. Opt. **4**, S140–S144 (2002).
10. P. A. Temple, "Total internal reflection microscopy: A surface inspection technique," Appl. Opt. **20**, 2656–2664 (1981).
11. A. Cvitkovic, N. Ocelic, and R. Hillenbrand, "Analytical model for quantitative prediction of material contrasts in

- scattering-type near-field optical microscopy," *Opt. Express* **15**, 8550–8565.
12. C. Girard, "Theoretical atomic-force-microscopy study of a stepped surface: Nonlocal effects in the probe," *Phys. Rev. B* **43**, 8822–8828 (1991).
 13. N. Gregersen, B. Tromborg, and S. Bozhevolnyi, "Vectorial modeling of near-field imaging with uncoated fiber probes: Transfer function and resolving power," *Appl. Opt.* **45**, 8739–8747 (2006).
 14. S. Wang, "Analysis of probe-sample interaction in near-field optical image of dielectric structure," *Microsc. Microanal.* **5**, 290–295 (1999).
 15. J.-C. Weeber, F. de Fornel, and J.-P. Goudonnet, "Numerical study of the tip-sample interaction in the photon scanning tunneling microscope," *Opt. Commun.* **126**, 285–292 (1996).
 16. D. Van Labeke and D. Barchiesi, "Probes for scanning tunneling optical microscopy: A theoretical comparison," *J. Opt. Soc. Am. A* **10**, 2193–2201 (1993).
 17. S. Bozhevolnyi, S. Berntsen, and E. Bozhevolnaya, "Extension of the macroscopic model for reflection near-field microscopy: Regularization and image formulation," *J. Opt. Soc. Am. A* **11**, 609–617 (1994).
 18. J.-J. Greffet and R. Carminati, "Image formulation in near-field optics," *Prog. Surf. Sci.* **56**, 133–237 (1997).
 19. A. Castiaux, H. Danzebrink, and X. Bouju, "Glass and silicon probes: A comparative theoretical study for near-field optical microscopy," *J. Appl. Phys.* **84**, 52–57 (1998).
 20. J. Sun, P. Carney, and J. Schotland, "Strong tip effects in near-field scanning optical tomography," *J. Appl. Phys.* **102**, 103103 (2007).
 21. L. Novotny, D. Pohl, and P. Regli, "Near-field, far-field and imaging properties of the 2D aperture SNOM," *Ultramicroscopy* **57**, 180–188 (1995).
 22. H. Furukawa and S. Kawata, "Analysis of image formation in a near-field scanning optical microscope: Effects of multiple scattering," *Opt. Commun.* **132**, 170–178 (1996).
 23. K. Tanaka, M. Tanaka, and T. Omoya, "Boundary integral equation for a two-dimensional simulator of a photon scanning tunneling microscopy," *J. Opt. Soc. Am. A* **15**, 1918–1931 (1998).
 24. S. Goumri-Said, L. Salomon, J. Dufour, and F. de Fornel, "Two-dimensional numerical simulations of photon scanning tunneling microscopy: Fourier modal method and *R*-matrix algorithm," *Opt. Quantum Electron.* **36**, 787–806 (2004).
 25. S. Goumri-Said, L. Salomon, J. Dufour, F. de Fornel, and A. Zayats, "Numerical simulations of photon scanning tunneling microscopy: Role of probe tip geometry in image formation," *Opt. Commun.* **224**, 245–258 (2005).
 26. F. Brezzi and C. Johnson, "On the coupling of boundary integral and finite element methods," *Calcolo* **16**, 189–201 (1979).
 27. G. N. Gatica and W. L. Wendland, "Coupling of mixed finite elements and boundary elements for linear and nonlinear elliptic problems," *Appl. Anal.* **63**, 39–75 (1996).
 28. G.-C. Hsiao, "The coupling of BEM and FEM—a brief review," in *Boundary Element X*, (Springer, 1988), Vol. 1, pp. 431–445.
 29. C. Johnson and J.-C. Nédélec, "On the coupling of boundary integral and finite element methods," *Math. Comput.* **35**, 1063–1079 (1980).
 30. T. Tran, "The *K*-operator and the Galerkin method for strongly elliptic equations on smooth curves: Local estimates," *Math. Comput.* **64**, 501–513 (1995).
 31. P. Persson and G. Strang, "A simple mesh generator in Matlab," *SIAM Rev.* **46**, 329–345 (2004).
 32. J. Jin, *The Finite Element Method in Electromagnetics*, (Wiley, 1993).
 33. J. Coyle, "Locating the support of objects contained in a two-layered background medium in two dimensions," *Inverse Probl.* **16**, 275–292 (2000).